Journal of
Polymer Materials

Tech Science Press

http://doi.org/10.32604/jpm.2026.086549

ARTICLE

A Highly Deformable, Low-Viscosity Photocurable Shape Memory Polymer Enabling Digital Light Processing-Based 4D Printing with Thermal-Magnetic Multi-Responsive Actuation

Yuxuan Qin[1,#], Shouyi Yu[2,#], Yunlong Guo[1], Ang Chu[1], Yilin Liu[1], Qi Ge[2,*] and Biao Zhang[1,*]

[1]State Key Laboratory of Flexible Electronics (LOFE) & School of Flexible Electronics (SFE), Northwestern Polytechnical University, 127 West Youyi Road, Xi'an, China
[2]Shenzhen Key Laboratory for Additive Manufacturing of High-Performance Materials, Department of Mechanical and Energy Engineering, Southern University of Science and Technology, Shenzhen, China
*Corresponding Authors: Qi Ge. Email: geq@sustech.edu.cn; Biao Zhang. Email: iambzhang@nwpu.edu.cn
#These authors contributed equally to this work

Received: 01 June 2026; Accepted: 09 September 2026; Published: 24 September 2026

ABSTRACT: 4D printing relies on smart materials capable of controlled deformation upon external stimuli. Existing photocurable shape memory polymers (SMPs) suffer from high viscosity, single (thermal) responsiveness, and insufficient deformability, which limit their applications. Herein, we report a low-viscosity, UV-curable SMP resin composed of tetrahydrofurfuryl acrylate, isobornyl acrylate, acryloylmorpholine as monomers and aromatic urethane dimethacrylate as crosslinker (TIA-AUD), with large deformability, tailor-made for digital light processing (DLP)-based 4D printing. We designed and synthesized a high-molecular-weight polyurethane based crosslinker with excellent properties. Through synergistic regulation of multiple reactive diluents to optimize resin performance, the material achieves outstanding high-temperature deformability (Elongation at break of 620% at 100°C) together with good room-temperature toughness (280% at 20°C), as well as shape fixity and recovery ratios of approximately 97% and 92%, respectively. Moreover, incorporation of Fe_3O_4 nanoparticles endows the material with magnetic responsiveness: under an alternating magnetic field, the composite undergoes inductive heating above its glass transition temperature, enabling untethered shape memory actuation with a recovery ratio of about 91%. This work provides a versatile SMP platform for DLP-based 4D printing that integrates low viscosity, high deformability, and multi-stimuli responsiveness, expanding the material portfolio for soft actuators and intelligent devices.

KEYWORDS: 4D printing; digital light processing (DLP); shape memory polymer (SMP); low viscosity; high deformability; multi-stimuli responsiveness; magnetic hyperthermia

1 Introduction

4D printing [1], as a novel smart additive manufacturing technology, introduces a time-dependent dynamic response mechanism [2] on the basis of the layer-by-layer stacking principle of conventional 3D printing. Unlike traditional static printing processes, this technology relies fundamentally on various types of specialty responsive composite materials, including shape memory polymers [3–5], hydrogels [6,7], elastomers [8], and the like. The as-fabricated components, requiring no post-printing manual secondary processing, can autonomously undergo a series of controllable dynamic responses, such as morphological shrinkage, stiffness modulation, and structural deformation, solely under external natural stimuli (e.g., temperature, mechanical load, and environmental humidity) [9], following a pre-designed structural

configuration. This capability overcomes the conventional manufacturing limitation that the structure and performance of traditional products remain fixed after fabrication. In terms of engineering applications, this technology holds substantial value for both practical deployment and research development. It can be used to fabricate industrial precision components capable of self-deformation to meet assembly requirements [10], develop wearable protective equipment that adaptively adjusts fit and support according to human body conditions [11], create flexible soft devices that autonomously alter their morphological structure in response to complex environments [12], and extend to fields such as medical rehabilitation adaptive components [13,14] and civil smart wearable products. Thus, it meets the core research and development demands of multiple industries for personalized customization, intelligent adaptation, and multifunctional dynamic regulation.

Among the various additive manufacturing techniques, digital light processing (DLP)-based vat photopolymerization [15–18] is particularly well-suited for fabricating 4D smart structures due to its high resolution, high efficiency, and ability to create complex geometries with minimal surface artifacts [19,20]. In DLP, a digital micromirror device projects the UV pattern of an entire layer at once, enabling rapid, one-step curing of photosensitive resins without the need for point-by-point scanning or nozzle extrusion. This technology therefore offers a solid foundation for achieving precise, repeatable, and programmable shape deformation in response to external stimuli.

Photocurable shape memory polymers (SMPs) are key smart polymeric materials in DLP-based 4D printing [21]. By introducing photosensitive reactive groups into the molecular chains of conventional shape memory polymers [22], these materials enable rapid UV crosslinking and curing while retaining stable shape memory characteristics, thereby making them compatible with DLP-based 4D printing processes. Current research in this field primarily focuses on acrylate systems [23–25] and/or epoxy-modified materials [26–28]. Acrylate-based materials offer rapid curing [29], high forming precision [30], and strong mechanical stability [31]. For example, Ge et al. [18] achieved multi-material 4D printing based on projection microstereolithography (PμSL). The as-fabricated methacrylate-based photocurable shape memory polymers exhibited tunable thermomechanical properties over a wide range, with an elongation at break of up to 300% and a shape fixity ratio exceeding 90%. Moreover, the temporal sequence of deformation could be accurately predicted by model-based design. Polyurethane materials for constructing photocurable SMPs exhibit excellent flexibility, good resilience, and stable cyclic deformation performance [32,33], making them suitable for fabricating bending-type structures. Zhang et al. [3] developed a tert-butyl acrylate-aliphatic urethane diacrylate (tBA-AUD) system compatible with DLP printing, demonstrating high curing efficiency, high resolution, and an elongation at break as high as 1240%, along with excellent fatigue resistance. This system significantly improved the mechanical properties and practicality of 4D-printed structures, offering high deformability and fatigue resistance. However, when the AUD content exceeded 50 wt%, the resin viscosity became too high for DLP printing, thereby limiting the tunability of material composition and performance [3]. Despite these advances, most existing photocurable SMPs still suffer from two major limitations: (i) they primarily rely on single-stimulus (typically thermal) actuation, lacking integrated multi-responsiveness [34,35]; and (ii) achieving both low resin viscosity and high deformability in a single system remains challenging, especially for DLP-based printing. Furthermore, the development of SMPs with remote and untethered controllability (e.g., magnetic or photo-induced actuation) is still in its early stage. Therefore, to achieve better application performance, we aim to develop a UV-curable SMP material system that features low viscosity, excellent deformability under both high- and low-temperature conditions, and multi-dimensional stimulus responsiveness (photo, thermal, and magnetic, etc.), thereby expanding the engineering applications of SMP in 4D printing.

In this study, a high molecular weight aromatic urethane dimethacrylate (AUD) was designed and synthesized. Through synergistic regulation of multiple reactive diluents, a low-viscosity, stable, non-volatile, and UV-curable shape memory polymer (SMP) material system was formulated. This system exhibits a high curing rate and is compatible with DLP-based 3D printing, enabling the fabrication of various complex structures with high precision. On this basis, the SMP system was further compounded with ferrosoferric oxide (Fe_3O_4) particles to obtain a hybrid material system that exploits magnetic-field-responsive characteristics, thereby establishing contactless shape memory actuation. This study aims to provide a designable and processable smart material for 4D printing, offering a potential solution for DLP-compatible SMPs with remote-controlled actuation.

2 Experimental Details

2.1 Materials

2,4-Toluene diisocyanate (2,4-TDI, 99%), poly(tetramethylene ether) glycol (PTMG, Mn = 2000), dibutyltin dilaurate (DBTDL), anhydrous ethyl acetate (99.5%), 1,4-butanediol (1,4-BDO, 99%), tetrahydrofurfuryl acrylate (THFA, 97%), isobornyl acrylate (IBOA, 96%), acryloylmorpholine (ACMO, 98%), Diphenyl(2,4,6-trimethylbenzoyl)phosphine oxide (TPO, 98%), Fe_3O_4 (99.5%), and Sudan I were purchased from Adamas. 2-Hydroxyethyl methacrylate (HEMA, 96%) was purchased from Macklin. All reagents were used as received without further purification.

2.2 Synthesis of AUD

In a three-necked flask, 0.1 mol of 2,4-TDI and 0.05 mol of PTMG-2000 were added to achieve an -NCO/-OH molar ratio of 2:1. Subsequently, 0.1 wt% DBTDL was introduced as the catalyst, and the mixture was heated to 85°C in an oil bath with mechanical stirring at 200 r/min for 3 h. During this period, urethane linkages formed and the viscosity increased gradually. The temperature was then lowered to 30°C, and 50 vol% ethyl acetate was added as a diluent. The mixture was stirred for 1 h to ensure complete dissolution and to prevent solvent evaporation and inhomogeneous mixing. The temperature was subsequently raised to 65°C, and 0.0375 mol of 1,4-BDO was added. The reaction was allowed to proceed under the same stirring conditions for another 3 h to consume a portion of the -NCO groups. Finally, 0.025 mol of HEMA was added to react with the remaining -NCO groups at 65°C and 200 r/min for 3 h. The reaction time for each step was predetermined through preliminary experiments to ensure complete consumption of the -NCO groups (Fig. S1). The resulting solution was transferred to an open glass Petri dish and dried under vacuum at 55°C for 24 h to remove the solvent, yielding the product. The final aromatic urethane dimethacrylate (AUD) product was characterized by ^{1}H Nuclear Magnetic Resonance Spectroscopy (Fig. S2) and FTIR spectroscopy (Fig. S3). The spectrum shows no detectable peak at ~2270 cm^{-1}, indicating that the -NCO groups were completely consumed.

2.3 Preparation of Precursor Solution

The synthesized AUD was mixed with the reactive THFA, IBOA, and ACMO in the proportions given in Table S1. The mixture was stirred thoroughly to obtain a low-viscosity resin precursor solution. TPO was added at 1 wt% of the total mass as a photoinitiator. For the printing of fine structures, Sudan I was additionally added at 0.05 wt% of the total polymer resin mass as a light absorber to suppress light scattering and improve printing resolution.

2.4 3D Printing Procedure

The 3D models of the printing structures were designed using SolidWorks 2018. The models were then imported into Chitubox slicing software, where each model was sliced into a series of image layers with a layer thickness of 0.1 mm. The resulting layer images were subsequently transferred to the MultiMatter C10 DLP-based 3D printing system. The printer is equipped with a 405 nm UV-LED light source. All printing experiments were conducted at an ambient temperature of 23 ± 2°C and a relative humidity of 45 ± 5%. The printed parameters for different structures were shown in Table S2 (Printing parameters for the TIA-AUD resin) and Table S3 (Printing parameters for the TIA-AUD-Fe resin), respectively.

After printing, the as-printed parts were centrifuged on the printer's build platform at 4000 r/min for 10 s to completely remove any uncured resin residue from both the surface and the internal voids of the hollow structures. This post-treatment step yielded clean samples for subsequent characterization.

2.5 Shape-Memory Behavior Tests

The shape memory behavior of the material was investigated via a typical shape memory cycle. A rectangular specimen with dimensions of 15 mm × 5 mm × 2 mm was first heated from room temperature to 80°C at a rate of 3°C/min, then bent to a desired angle under external force, and the bending angle at this state was recorded as α. Subsequently, the specimen was rapidly cooled to 0°C at a rate of 5°C/min to fix the temporary shape. After the temperature stabilized and the specimen was held at 0°C for 2 min, the bending angle was recorded as β. In the free recovery step, the specimen was reheated to 80°C at a rate of 3°C/min and held at this temperature for 10 min until the shape stabilized, and the final bending angle was recorded as γ. The shape fixation ratio (R_f) and shape recovery ratio (R_r) of the material were calculated based on the above angular data. The calculation formulas are expressed as follows:

$$R_f = \frac{\beta}{\alpha} \times 100\% \tag{1}$$

$$R_r = \frac{\beta - \gamma}{\beta} \times 100\% \tag{2}$$

R_f is defined as the ratio of the strain retained after unloading and cooling to the maximum strain before unloading, representing the ability of the material to lock its temporary shape. R_r is defined as the ratio of the recovered strain upon reheating to the maximum strain before unloading, representing the degree to which the material returns to its original shape.

2.6 Characterization

2.6.1 ^{1}H Nuclear Magnetic Resonance Spectroscopy (^{1}H NMR)

^{1}H NMR Spectrum of AUD was recorded on a Bruker AVANCE NEO 500 spectrometer at room temperature using acetone-d_6 as the solvent, as shown in Fig. S2.

2.6.2 Dynamic Mechanical Analysis (DMA)

Dynamic Mechanical Analysis (DMA) was performed on a Netzsch DMA 242E in tension mode. All specimens were cut precisely to dimensions of 8 mm × 5 mm × 1 mm (length × width × thickness). The measurements were carried out at a frequency of 1 Hz, an amplitude of 50.0 μm, over a temperature range from −50°C to 150°C at a heating rate of 3°C/min.

2.6.3 Mechanical Properties

Tensile properties were measured with a ZST6502 universal testing machine. The resin precursor solution was poured into a silicone mold conforming to GB/T 528-2009 and fully cured in a light-curing chamber at a light intensity of 1 W/cm^2 for 1 h to obtain dumbbell-shaped specimens with a gauge section of 10 mm × 2 mm × 1.8 mm. The tensile test was performed at a crosshead speed of 10 mm/min. Each sample was tested three times, and the average value was reported.

2.6.4 Fourier Transform Infrared Spectroscopy (FTIR)

FTIR spectra were recorded on a Bruker Tensor II spectrometer (Germany) equipped with an ATR accessory. All spectra were collected in the range of 4000–500 cm^{-1} with a resolution of 4 cm^{-1} and 32 scans. Liquid resin samples were measured directly using the ATR mode. Solid cured polymer samples and the purified AUD product were measured similarly after being placed onto the ATR crystal.

3 Results and Discussion

The TIA-AUD shape memory polymer (SMP) system investigated in this work consists of three reactive diluents, namely tetrahydrofurfuryl acrylate (THFA), isobornyl acrylate (IBOA), and acryloylmorpholine (ACMO), along with a self-synthesized aromatic urethane dimethacrylate (AUD) crosslinker, using diphenyl(2,4,6-trimethylbenzoyl)phosphine oxide (TPO) as the photoinitiator. The molecular structures of each component are presented in Fig. 1a,b. AUD, as a high-molecular-weight crosslinker, features a long-chain polyurethane backbone that significantly increases the distance between crosslinking points, thereby endowing the material with high deformability. Among the three diluents, IBOA provides a high glass transition temperature (T_g) and mechanical strength owing to its rigid isobornyl group; ACMO modulates network rigidity and hydrogen-bonding density through its strongly polar amide group; and THFA, whose homopolymer exhibits a low T_g (approximately −15°C), introduces segmental flexibility into the copolymer network, enabling the material to possess both glassy toughness and rubbery high extensibility. Their synergistic action also effectively reduces the precursor viscosity, meeting the rheological requirements of digital light processing (DLP) printing (Fig. 1a).

The shape memory behavior of the TIA-AUD system is based on a thermal transition mechanism. As illustrated in Fig. 1c, upon irradiation with 405 nm UV light, TPO decomposes to generate free radicals, initiating the polymerization of acrylate and/or methacrylate groups and converting the liquid precursor into a chemically crosslinked solid network. The permanent crosslinking points provided by the AUD crosslinker store the information of the original shape. When the temperature is raised above T_g, the segmental motion is activated, the material enters the rubbery state, and an external force is applied to deform it into a temporary shape. Immediately thereafter, the external force is removed, and the system is cooled below T_g, whereupon the segmental motion is frozen, and the temporary shape is stably fixed. Upon reheating above T_g, the segmental mobility is restored, and the crosslinked network drives the sample to spontaneously recover to its permanent shape. This complete shape memory cycle has been visually verified by the photographs shown in Fig. 1d.

The photocuring reaction of the TIA-AUD system was verified by Fourier-transform infrared spectroscopy (FTIR). Fig. 2a compares the FTIR spectra of the liquid printing ink and the UV-cured polymer. After curing, the characteristic absorption peak of the C=C stretching vibration at approximately 1620 cm^{-1} diminished significantly, indicating that the acrylate double bonds underwent efficient free-radical polymerization upon photoinitiation. Furthermore, intermolecular hydrogen bonds can form between the strongly polar amide groups of ACMO and the carbamate groups (–NH–COO–) of the AUD chains, as well as the

ether oxygen atoms of the THFA tetrahydrofuran ring (as shown in Fig. 2b). This physical crosslinking effect was indirectly corroborated by subsequent mechanical and thermodynamic analyses.

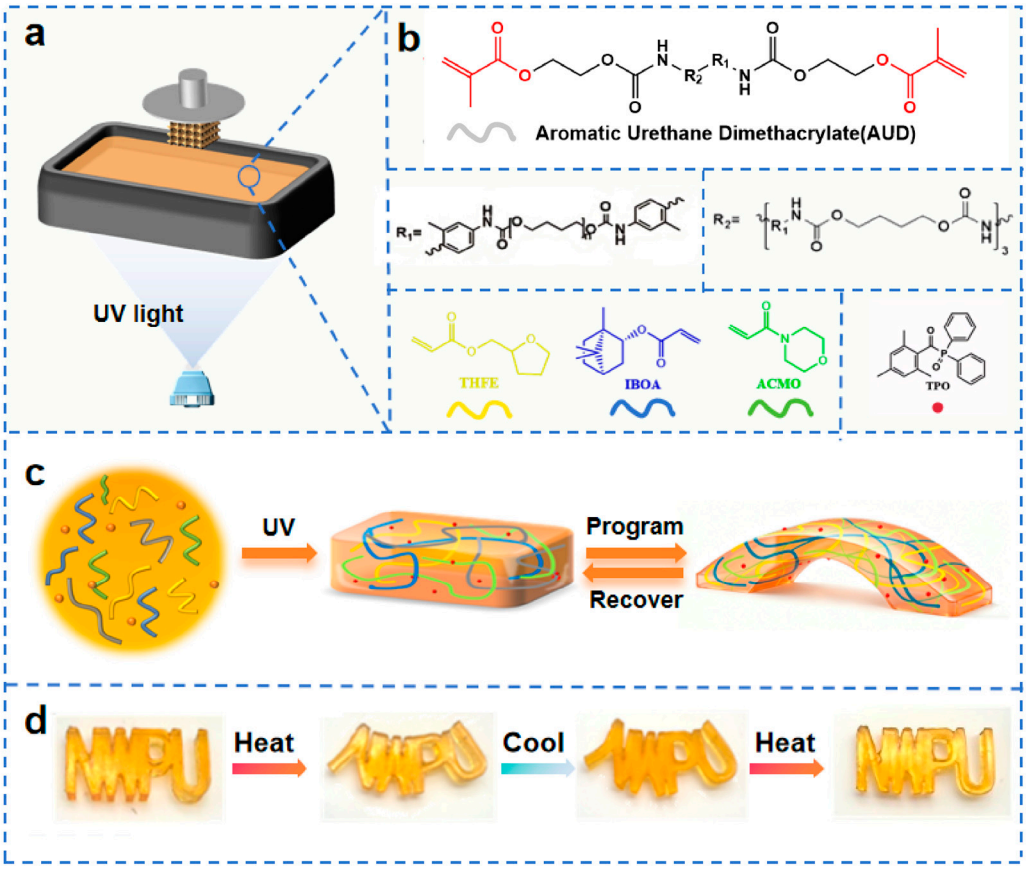

Figure 1: (**a**) Schematic illustration of DLP-based 3D printing. (**b**) Chemical structures of the TIA-AUD shape memory polymer components. (**c**) Schematic illustration of photopolymerization and thermal-induced shape memory cycle. (**d**) Photographs demonstrating the shape memory process.

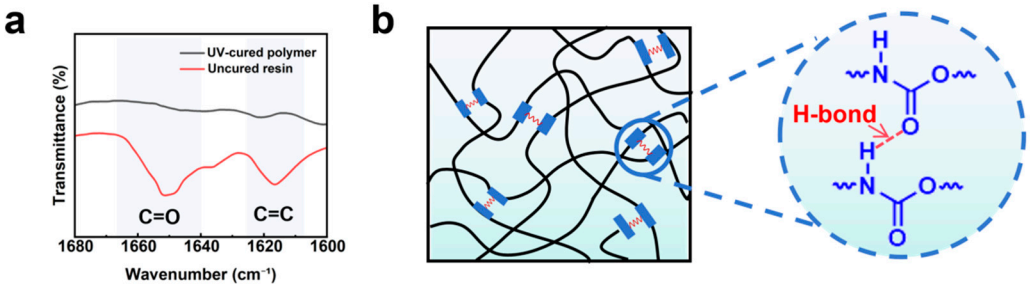

Figure 2: *Cont.*

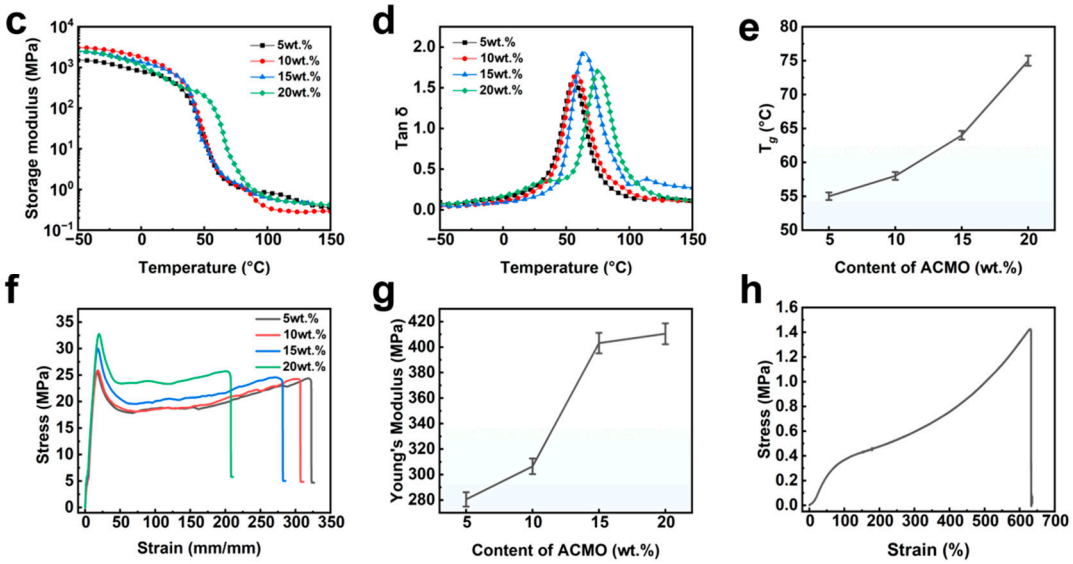

Figure 2: (**a**) FTIR spectra comparison of the liquid printing ink and UV-cured polymer. (**b**) Schematic illustration of intermolecular hydrogen bonding. (**c**) DMA curves of storage modulus (E′) as a function of temperature for different ACMO contents. (**d**) DMA curves of loss factor (tan δ) as a function of temperature. (**e**) Glass transition temperature (T_g) as a function of ACMO content. (**f**) Uniaxial tensile stress-strain curves at room temperature (20°C) for formulations with different ACMO contents. (**g**) Young's modulus as a function of ACMO content. (**h**) Uniaxial tensile stress-strain curve at 100°C for the optimal formulation (with 15 wt% ACMO).

To determine the optimal formulation for further systematic characterization, we fixed the AUD crosslinker content at 15 wt% and varied the ACMO content (5, 10, 15 and 20 wt%, respectively). Dynamic mechanical thermal analysis (DMA) and uniaxial tensile tests were performed on the four TIA-AUD formulations. Fig. 2c,d presents the storage modulus (E′) and loss factor (tan δ) as functions of temperature, respectively. The glass transition temperature (T_g) of each formulation was determined from the peak of tan δ, and the trend of T_g with ACMO content is summarized in Fig. 2e. With increasing ACMO content, T_g gradually increased, Fig. 2f shows the uniaxial tensile stress–strain curves at room temperature (20°C) for the four formulations. As the ACMO content increased from 5 wt% to 20 wt%, both the initial modulus and the fracture strength progressively increased, whereas the elongation at break monotonically decreased: the 5 wt% group exhibited the largest elongation at break (≈330%) but the lowest strength (≈24 MPa), while the 20 wt% group showed the highest strength (≈33 MPa) with a significantly reduced elongation at break of 210%. The Young's modulus extracted from the tensile data is plotted against ACMO content in Fig. 2g, exhibiting a monotonic increasing trend that positively correlates with the change of T_g. The microscopic mechanism underlying these trends probably lies in the formation of intermolecular hydrogen bonds among the strongly polar amide groups of ACMO, the carbamate groups of AUD, and the ether oxygen atoms of THFA. These hydrogen bonds serve as physical crosslinking points and synergistically construct a multi-level network together with the chemical crosslinks provided by AUD. Higher ACMO content leads to higher hydrogen-bond density and stronger physical crosslinking. This brings a dual effect: the positive effect is enhanced network rigidity and thermal stability (increased modulus and T_g), the negative effect is restricted cooperative orientation and slippage of chain segments under external force, resulting in a decreased elongation at break. This result exemplifies a typical stiffness-toughness trade-off, where the

ACMO content essentially modulates the relative contribution of hydrogen-bond physical crosslinking versus chemical crosslinking in the network.

A comprehensive comparison of the mechanical and thermodynamic properties of the four formulations reveals that the 15 wt% ACMO group achieves the best balance among rigidity, toughness, and thermal stability. Therefore, it was selected as the target formulation for subsequent shape memory performance studies. Notably, this optimal formulation still maintains an elongation at break of 280% in the glassy state (Fig. 2f), and this favorable low-temperature toughness ensures the structural reliability of the temporary shape. Based on this optimal formulation, we further investigated its deformation capability at elevated temperatures. DMA measurement gave a T_g of approximately 65°C for this formulation. The elongation at break increases with temperature (Fig. S4). Fig. 2h presents the uniaxial tensile stress–strain curve at 100°C (rubbery state), where the material exhibits an elongation at break as high as 640%. Equilibrium swelling experiments were performed to complement the network structure analysis, and the corresponding swelling kinetics data are presented in the Supporting Information (Figs. S5 and S6). The apparent crosslinking density of the TIA-AUD network was further estimated from the rubbery plateau modulus obtained by DMA measurements, with detailed calculation provided in the Supporting Information [36] (Table S4). These results collectively confirm the large crosslink spacing of the TIA-AUD network. This excellent high-temperature deformability provides ample deformation space for the programming process.

The printability of the TIA-AUD ink via DLP technology was systematically evaluated. To suppress UV light scattering in the resin and enhance in-plane resolution, 0.05 wt% Sudan I was added as a photoabsorber. Through repeated testing, the minimum achievable feature size of this system was determined to be 50 μm. As demonstrated in Fig. 3, the ink successfully fabricates a two-dimensional honeycomb network (Fig. 3a) and its magnified microstructure (Fig. 3b), as well as a variety of centimeter-scale three-dimensional complex structures (Fig. 3c–h). From one-dimensional lines at micron precision to two-dimensional grids and further to macroscopic three-dimensional components, the TIA-AUD system exhibits excellent cross-scale printability, enabling accurate fabrication from micron to centimeter scales.

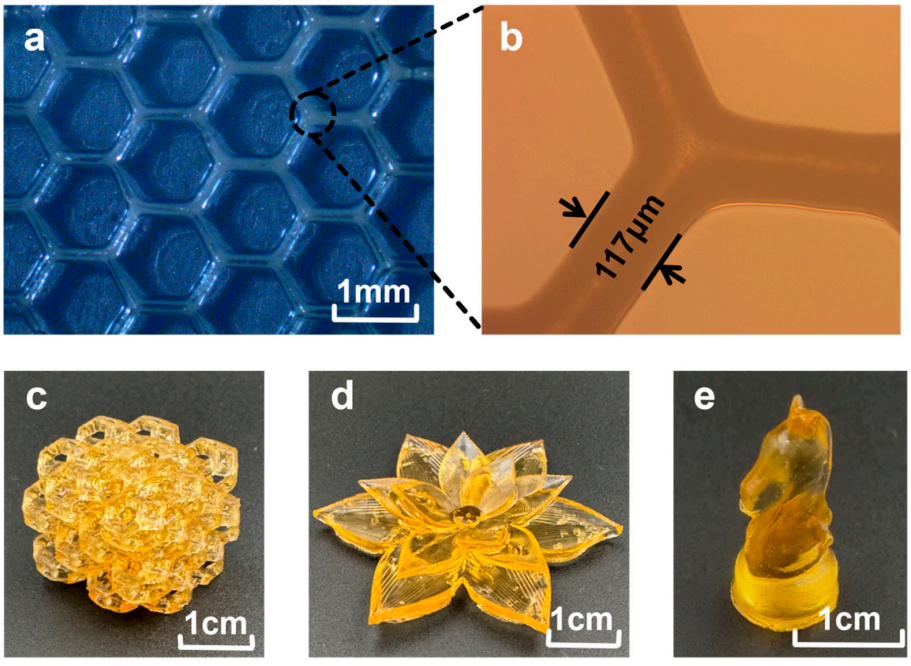

Figure 3: *Cont.*

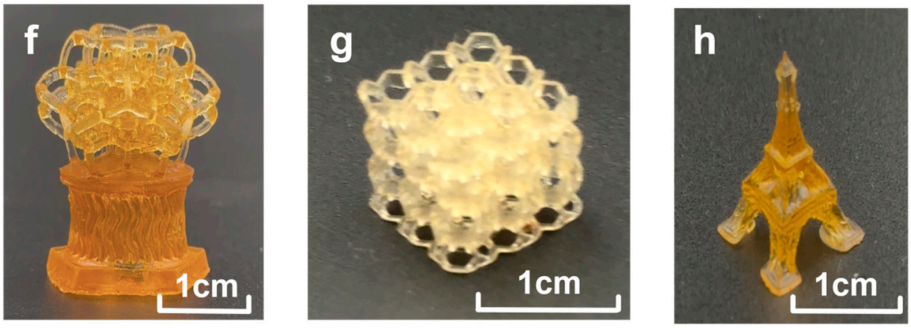

Figure 3: DLP printability evaluation of the TIA-AUD ink. (**a**) The two-dimensional honeycomb network structure and (**b**) the magnified view of the microstructure. (**c**–**h**) various centimeter-scale three-dimensional complex structures. Scale bars: 1 mm and 1 cm as indicated.

The shape memory behavior of the TIA-AUD system was first visually verified by macroscopic deformation demonstrations of the printed structures. Fig. 4a presents various structures printed with the 15 wt% ACMO formulation, illustrating the four typical stages of the shape memory cycle: initial permanent shape → deformation upon heating (programming) → temporary shape fixation upon cooling → recovery to the initial shape upon reheating. The programming and the recovery temperature was 80°C, while the fixation temperature was 0°C, and the recovery temperature was 80°C. As observed, multiple complex structures underwent substantial bending deformation at the programming temperature, stably locked into the temporary configuration after cooling, and rapidly recovered to their original shape upon reheating, with no significant residual deformation.

Fig. 4b,c presents the shape fixation ratio (R_f) and shape recovery ratio (R_r) of four formulations with different ACMO contents. The R_f values of all groups remain around 97%, indicating that ACMO content exerts negligible influence on shape fixation capacity. This result demonstrates that the networks of various formulations can effectively retain temporary deformation under the glassy state. The R_r fluctuates slightly with the rising ACMO content and maintains a relatively high level of approximately 92%. A decline in recovery ratio is observed for the 20 wt.% group, which may be attributed to irreversible slippage of partial chain segments during programming induced by excessively high hydrogen bond density.

Based on the optimal formulation (with 15 wt.% ACMO), Fe_3O_4 nanoparticles at different contents (1 and 3 wt.%) were introduced into the TIA-AUD system and uniformly dispersed in the resin matrix by mechanical stirring and ultrasonication (Fig. 5a). Rheological measurements (Fig. 5b) show that the ink viscosity increases with increasing Fe_3O_4 content; nevertheless. Even all formulations exhibit typical shear-thinning behavior, the low viscosity facilitates rapid resin leveling during DLP printing and ensures process stability. A variety of structures, including a 2D mesh and two 3D architectures, were successfully fabricated by DLP (Fig. 5c). The printed samples display clear edges and no interlayer defects, indicating that the addition of Fe_3O_4 up to 3 wt% does not significantly compromise printing resolution.

The effects of Fe_3O_4 content on the thermomechanical and room-temperature mechanical properties were investigated by dynamic mechanical thermal analysis (DMA) and uniaxial tensile tests (Fig. 5d–h). With increasing Fe_3O_4 loading, the glass transition temperature (T_g) gradually decreases (Fig. 5f), accompanied by a decreasing trend in both the upper yield strength and Young's modulus (Fig. 5g,h). The DMA and tensile data corroborate each other, consistently indicating that the incorporation of Fe_3O_4 weakens the structural integrity of the polymer network. UV-V is transmission results indicate that the black Fe_3O_4 particles possess strong light absorption during UV curing, competing with the photoinitiator for incident photons and reducing the penetration depth, thereby leading to a lower crosslinking density and consequently a reduced

T_g. (Fig. S7). Notably, all Fe_3O_4-containing samples maintain an elongation at break of approximately 280%, comparable to that of the neat resin, indicating that the material retains good ductility and can meet large-deformation application requirements.

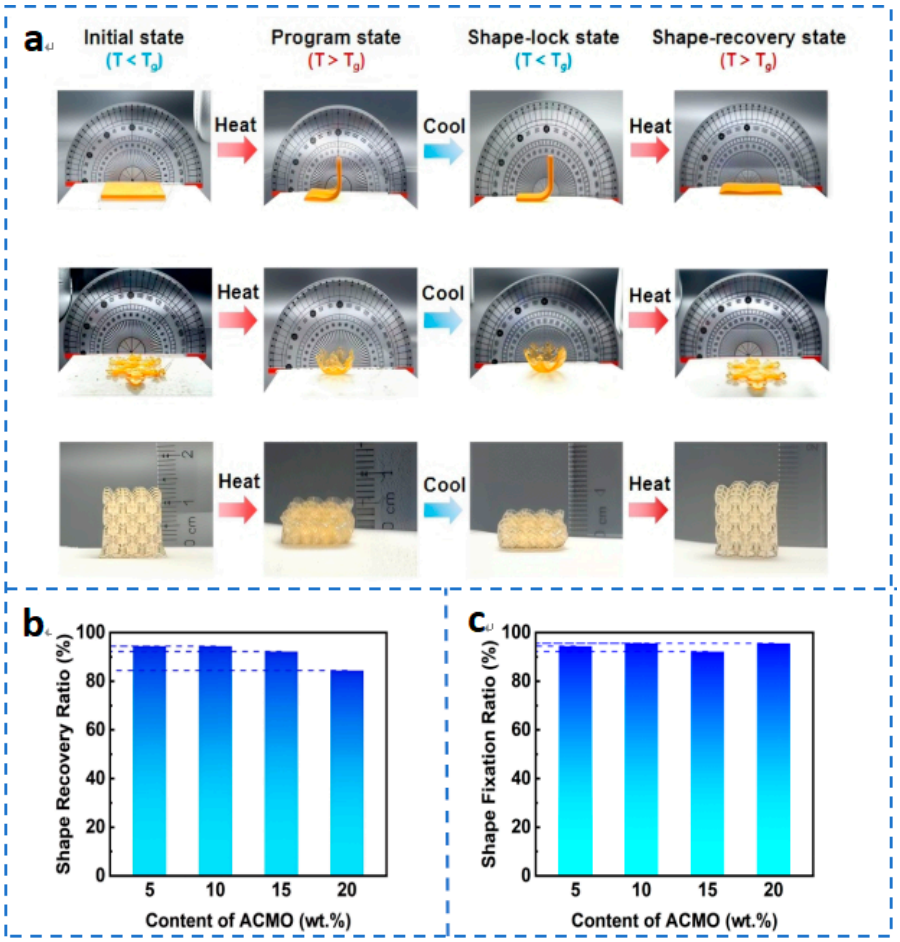

Figure 4: (**a**) Photographs of various structures printed with the 15 wt% ACMO formulation at the four typical stages of the shape memory cycle. (**b**) Shape recovery ratio (R_r) as a function of ACMO content. (**c**) Shape fixation ratio (R_f) as a function of ACMO content.

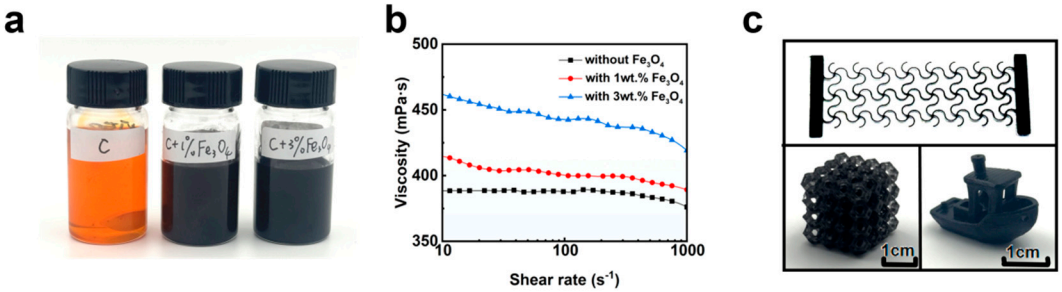

Figure 5: *Cont.*

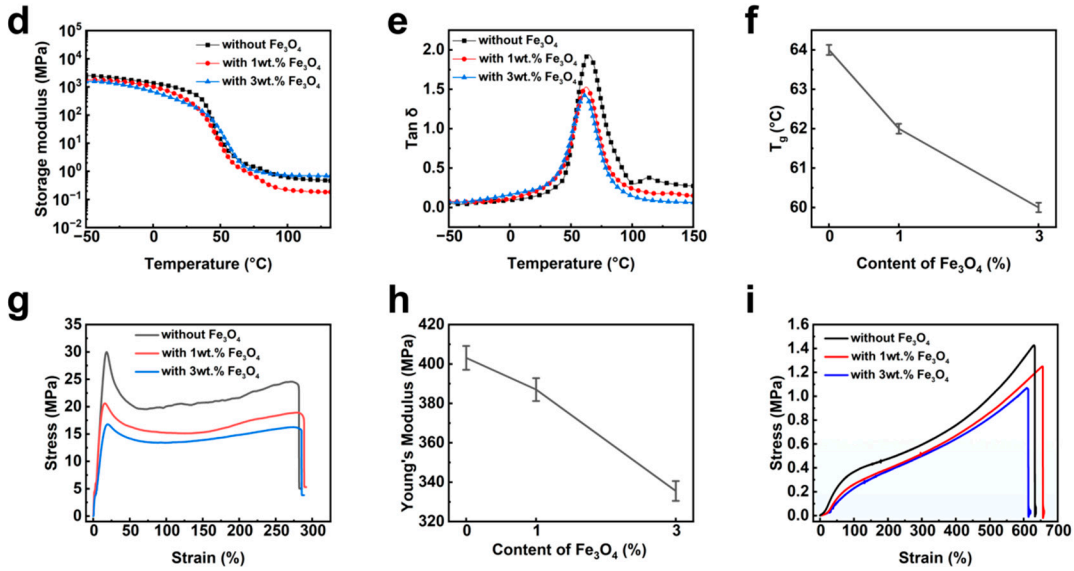

Figure 5: (**a**) Photographs of printing inks with 0%, 1 wt% and 3 wt% Fe_3O_4 respectively. (**b**) Viscosity as a function of shear rate for inks with different Fe_3O_4 contents. (**c**) DLP-printed structures using the resin containing 1 wt% Fe_3O_4: a 2D mesh and two 3D structures. (**d**) Storage modulus (E′) as a function of temperature from DMA for formulations with different Fe_3O_4 contents. (**e**) Loss factor (tan δ) as a function of temperature from DMA. (**f**) Glass transition temperature (T_g) as a function of Fe_3O_4 content. (**g**) Uniaxial tensile stress-strain curves at room temperature (20°C) for different Fe_3O_4 contents. (**h**) Young's modulus as a function of Fe_3O_4 content. (**i**) Uniaxial tensile stress-strain curves at 100°C for different Fe_3O_4 contents.

At the programming temperature of 100°C, all Fe_3O_4-containing samples exhibit excellent high-temperature deformability (Fig. 5i), with elongations at break remaining around 640%, providing ample deformation margin for subsequent magnetically induced actuation.

Based on the comprehensive evaluation of the mechanical and thermodynamic properties described above, the TIA-AUD-Fe system with 1 wt.% Fe_3O_4 was selected for magnetically responsive shape memory testing. Taking advantage of the magnetic hyperthermia effect of Fe_3O_4 nanoparticles, the non-contact actuation capability of this system under an alternating magnetic field was investigated. The experimental setup is shown in Fig. 6a, where the sample was fixed to the test platform using adhesive tape and placed in an alternating magnetic field, while its surface temperature was monitored in real time by an infrared thermal camera. Fig. 6b presents the temperature evolution at the sample center as a function of time under different input powers. With increasing power, both the heating rate and the steady-state temperature increased significantly, indicating that Fe_3O_4 nanoparticles effectively convert magnetic energy into heat through hysteresis loss and relaxation losses (including Néel and Brownian relaxation) under the alternating magnetic field. Fig. 6c shows the shape recovery ratio as a function of time under different input powers. Once the sample temperature exceeds the glass transition temperature ($T_g \approx 62$°C), the material enters the rubbery state, segmental mobility is substantially enhanced, and the pre-programmed temporary shape begins to recover rapidly. Consequently, higher input power leads to a shorter time to reach T_g and a faster recovery rate. The final recovery ratios under the three power levels all reach approximately 91%, representing a reasonably satisfactory level. It should be noted that the sample was fixed with adhesive tape, and the boundary constraints imposed by the tape have a certain influence on the shape recovery ratio. The photographs and infrared thermal images in Fig. 6d,e visually illustrate the shape recovery process:

the rectangular strip returns from a folded state to a flat state, while the petal-shaped structure gradually expands from a contracted state upon thermal triggering to recover its original morphology. The videos are shown in Movies S1–S4. These results demonstrate that the incorporation of an appropriate amount of Fe_3O_4 endows the TIA-AUD system with remote, rapid, and controllable magnetically responsive shape memory functionality, achieving non-contact shape memory actuation.

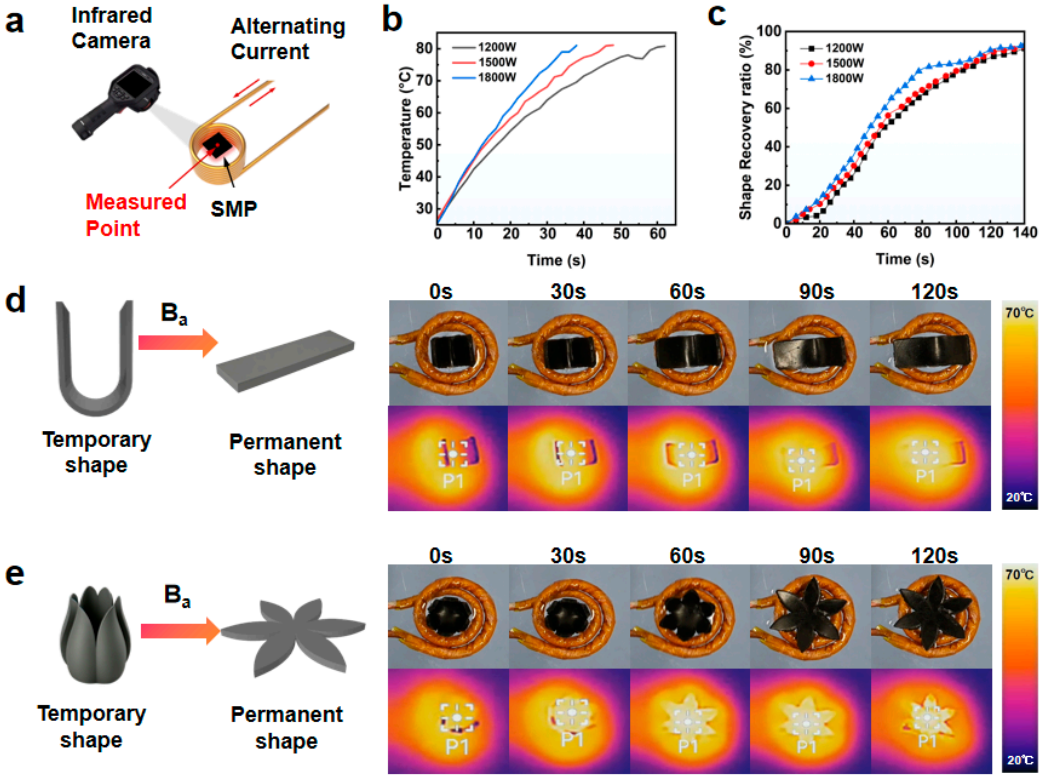

Figure 6: (**a**) Schematic diagram of the magnetically induced actuation experimental setup. (**b**) Temperature at the sample center as a function of time under different input powers. (**c**) Shape recovery ratio as a function of time under different input powers. (**d**,**e**) Photographs and infrared thermal images during the shape recovery process under magnetic actuation with an input power of 1200 W (d: a rectangular strip recovering from a folded state to a flat state. e: a petal-shaped structure recovering from a contracted state upon heating).

4 Conclusion

In summary, we have developed a highly deformable, low-viscosity UV-curable shape memory polymer resin suitable for DLP-based 4D printing. By synergistically regulating multiple reactive diluents, the resin overcomes the common issues of high viscosity and single thermal responsiveness found in conventional photocurable SMP systems. The resin exhibits good fluidity at room temperature and demonstrates excellent cross-scale printability. The optimized formulation (with 15 wt.% ACMO) combines low-temperature toughness (elongation at break of 280% at 20°C) with excellent high-temperature large deformability (620% at 100°C), along with stable shape fixity (≈97%) and recovery (≈92%) ratios. Upon incorporation of Fe_3O_4 nanoparticles, the material enables non-contact shape memory actuation under an alternating magnetic field (recovery ratio ≈91%) through the magnetic hyperthermia effect, further endowing the material with multi-stimuli responsiveness and expanding the stimulus-response dimensionality of SMPs. This material system provides a versatile platform for DLP-based 4D printing that integrates low viscosity, large

deformability, and multi-responsiveness, showing promise for applications in soft actuators and untethered smart devices.

Acknowledgement: Not applicable.

Funding Statement: This research was supported by the Natural Science Basic Research Program of Shaanxi (Program No. 2025JC-YBMS-358).

Author Contributions: The authors confirm contribution to the paper as follows: conceptualization, Yuxuan Qin and Shouyi Yu; methodology, Yuxuan Qin and Shouyi Yu; software, Yuxuan Qin; validation, Yuxuan Qin, Shouyi Yu and Yunlong Guo; formal analysis, Yuxuan Qin; investigation, Yuxuan Qin and Shouyi Yu; resources, Yuxuan Qin and Yunlong Guo; data curation, Yuxuan Qin; writing—original draft preparation, Yuxuan Qin; writing—review and editing, Yuxuan Qin, Shouyi Yu and Yilin Liu; visualization, Yuxuan Qin and Ang Chu; supervision, Qi Ge and Biao Zhang; project administration, Qi Ge and Biao Zhang; funding acquisition, Qi Ge and Biao Zhang. All authors reviewed and approved the final version of the manuscript.

Availability of Data and Materials: The data presented in this study are available from the corresponding author upon reasonable request.

Ethics Approval: Not applicable.

Conflicts of Interest: Given Qi Ge and Biao Zhang's role as editorial board member of this journal, they had no involvement in the peer review of this article and had no access to information regarding its peer review. Full responsibility for the editorial process for this article was delegated to another journal editor. The authors declare no other conflicts of interest.

Supplementary Materials: The supplementary material is available online at https://www.techscience.com/doi/10.32604/jpm.2026.086549/s1.

References

1. Arsuffi B, Magrini T, Champeau M, Siqueira G, Titotto S. 4D printing of natural materials: a review. Sustain Mater Technol. 2025;44:e01346. [CrossRef].
2. Wu JJ, Huang LM, Zhao Q, Xie T. 4D printing: history and recent progress. Chin J Polym Sci. 2018;36(5):563–75. [CrossRef].
3. Zhang B, Li H, Cheng J, Ye H, Sakhaei AH, Yuan C, et al. Mechanically robust and UV-curable shape-memory polymers for digital light processing based 4D printing. Adv Mater. 2021;33(27):2101298. [CrossRef].
4. Xia Y, He Y, Zhang F, Liu Y, Leng J. A review of shape memory polymers and composites: mechanisms, materials, and applications. Adv Mater. 2021;33(6):e2000713. [CrossRef].
5. Li H, Zhang B, Ye H, Jian B, He X, Cheng J, et al. Reconfigurable 4D printing via mechanically robust covalent adaptable network shape memory polymer. Sci Adv. 2024;10(20):eadl4387. [CrossRef].
6. Liu B, Li H, Meng F, Xu Z, Hao L, Yao Y, et al. 4D printed hydrogel scaffold with swelling-stiffening properties and programmable deformation for minimally invasive implantation. Nat Commun. 2024;15(1):1587. [CrossRef].
7. Yang C, Boorugu M, Dopp A, Ren J, Martin R, Han D, et al. 4D printing reconfigurable, deployable and mechanically tunable metamaterials. Mater Horiz. 2019;6(6):1244–50. [CrossRef].
8. Yang R, Zhao Y. Non-uniform optical inscription of actuation domains in a liquid crystal polymer of uniaxial orientation: an approach to complex and programmable shape changes. Angew Chem Int Ed. 2017;56(45):14202–6. [CrossRef].
9. Yu YY, Xiang HP, Fan LF, Zhang MQ. Shape memory elastomers: a review of molecular structures, stimulus mechanisms, and emerging applications. Polym Sci Technol. 2025;1(4):271–98. [CrossRef].
10. Homssi R, Vallejo Ciro MI, Carvajal Loaiza MJ, Patterson AE, Restrepo V. Thermally recoverable PLA/TPU hooks for durable 4D-printed mechanical interlocks. Smart Mater Struct. 2026;35(5):055029. [CrossRef].

11. Ren L, Wu Q, Liu Q, Hao P, Tang J, Li J, et al. Stiffness-tunable and self-sensing integrated soft machines based on 4D printed conductive shape memory composites. Mater Des. 2023;228:111851. [CrossRef].
12. Joshi A, Choudhury S, Majhi A, Parasuram S, Baghel VS, Chauhan S, et al. 4D-printed multifunctional hydrogels as flexible strain sensors and nerve conduits. Biomater Sci. 2025;13(17):4706–16. [CrossRef].
13. Kanaujia KA, Yadav VK, Yadav SS, Talha M, Saraf SA, Kumar S. 4D printing in healthcare: innovations, challenges, and future directions. ACS Appl Bio Mater. 2026;9(2):493–528. [CrossRef].
14. Liu FK, Lu Z, Cui JJ, Guo YL, Liang C, Feng SW, et al. 4D printing micelle-enhanced shape memory polymer for minimally invasive implant. Chin J Polym Sci. 2025;43(11):1991–9. [CrossRef].
15. Ben Said L, Ayadi B, Alharbi S, Dammak F. Recent advances in additive manufacturing: a review of current developments and future directions. Machines. 2025;13(9):813. [CrossRef].
16. Cheng J, Yu S, Wang R, Ge Q. Digital light processing based multimaterial 3D printing: challenges, solutions and perspectives. Int J Extreme Manuf. 2024;6(4):042006. [CrossRef].
17. Swetha S, Sahiti TJ, Priya GS, Harshitha K, Anil A. Review on digital light processing (DLP) and effect of printing parameters on quality of print. Interactions. 2024;245(1):178. [CrossRef].
18. Ge Q, Sakhaei AH, Lee H, Dunn CK, Fang NX, Dunn ML. Multimaterial 4D printing with tailorable shape memory polymers. Sci Rep. 2016;6:31110. [CrossRef].
19. Li X, Cui G, Xu G. The principle and development of optical maskless lithography based digital micromirror device (DMD). Micromachines. 2025;16(12):1356. [CrossRef].
20. Sarabia-Vallejos MA, Rodríguez-Umanzor FE, González-Henríquez CM, Rodríguez-Hernández J. Innovation in additive manufacturing using polymers: a survey on the technological and material developments. Polymers. 2022;14(7):1351. [CrossRef].
21. Pittala RK, Torres MA, Reddy N, Swank S, Ecker M. Four-dimensional printing of shape memory polymers for biomedical applications: advances in DLP and SLA manufacturing. Polymers. 2026;18(1):24. [CrossRef].
22. Kumar SV, George JJ, Gopakumar D, Rani S, Sharma P, Gupta V, et al. Photo-responsive shape memory polymers: a critical review of synthesis, actuation principles, and functional applications. J Macromol Sci Part A. 2025;62(10):843–78. [CrossRef].
23. Cortés A, Cosola A, Sangermano M, Campo M, González Prolongo S, Pirri CF, et al. DLP 4D-printing of remotely, modularly, and selectively controllable shape memory polymer nanocomposites embedding carbon nanotubes. Adv Funct Mater. 2021;31(50):2106774. [CrossRef].
24. Zarek M, Layani M, Cooperstein I, Sachyani E, Cohn D, Magdassi S. 3D printing of shape memory polymers for flexible electronic devices. Adv Mater. 2016;28(22):4449–54. [CrossRef].
25. Karger-Kocsis J, Kéki S. Review of progress in shape memory epoxies and their composites. Polymers. 2017;10(1):34. [CrossRef].
26. Kausar A. Incipient shape memory featuring nano-reinforced epoxy nanocomposites—structural diversity and innovations. Polym Plast Technol Mater. 2024;63(9):1209–26. [CrossRef].
27. Shahi K, Ramachandran V, Mohan R, Ramachandran B. Shape memory properties of short-glass fiber reinforced epoxy composite programmed below glass transition temperature. J Polym Mater. 2025;42(2):477–96. [CrossRef].
28. Shi J, Zheng T, Yuan J, Qiu C, Ha Y, Zhang H, et al. Designing a self-healing shape memory polymer with high stiffness and toughness: the role of nonuniform chain networks. Macromolecules. 2024;57(23):10987–95. [CrossRef].
29. Rylski AK, Maraliga T, Wu Y, Recker EA, Arrowood AJ, Sanoja GE, et al. Digital light processing 3D printing of soft semicrystalline acrylates with localized shape memory and stiffness control. ACS Appl Mater Interfaces. 2023;15(28):34097–107. [CrossRef].
30. Jurinovs M, Veseta M, Sabalina A, Silva PES, Linarts A, Baniasadi H, et al. Sustainable 4D printable biobased shape memory polymers with linear tunability and multistimuli actuation for advanced applications. Small Sci. 2025;5(7):2500104. [CrossRef].
31. Delarue AP, McAninch IM, Peterson AM, Hansen CJ. Increasing printable solid loading in digital light processing using a bimodal particle size distribution. 3D Print Addit Manuf. 2024;11(5):e1819–28. [CrossRef].
32. Wang T, Liu Z, Jian F, Shen X, Wang C, Bian H, et al. Body temperature programmable shape memory thermoplastic rubber. J Polym Mater. 2025;42(1):81–94. [CrossRef].

33. Wu H, Chen P, Yan C, Cai C. Four-dimensional printing of a novel acrylate-based shape memory polymer using digital light processing. Mater Des. 2019;171:107704. [CrossRef].
34. Sánchez CP, Jérôme C, Noels L, Vanderbemden P. Review of thermoresponsive electroactive and magnetoactive shape memory polymer nanocomposites. ACS Omega. 2022;7(45):40701–23. [CrossRef].
35. Hassan H, Hallez H, Thielemans W, Vandeginste V. A review of electro-active shape memory polymer composites: materials engineering strategies for shape memory enhancement. Eur Polym J. 2024;208:112861. [CrossRef].
36. Hill LW. Calculation of crosslink density in short chain networks. Prog Org Coat. 1997;31(3):235–43. [CrossRef].